Journal of Materials Chemistry B

Thermo- and Ion-responsive Silk-elastin-like Proteins and Their Multiscale Mechanisms

Journal:	*Journal of Materials Chemistry B*
Manuscript ID	TB-ART-05-2022-001002.R1
Article Type:	Paper
Date Submitted by the Author:	12-Jul-2022
Complete List of Authors:	Shi, Haoyuan; Cornell University, Sibley School of Mechanical and Aerospace Engineering Ji, Ting; Zhejiang University School of Medicine, The Zhejiang University–University of Edinburgh Institute Zhai, Chenxi; Cornell University, Sibley School of Mechanical and Aerospace Engineering Lu, Junting; Zhejiang University School of Medicine, The Zhejiang University–University of Edinburgh Institute Huang, Wenwen; Zhejiang University School of Medicine, The Zhejiang University–University of Edinburgh Institute; Zhejiang University School of Medicine, Department of Orthopedics of the Second Affiliated Hospital; Zhejiang University School of Medicine, Dr. Li Dak Sum & Yip Yio Chin Center for Stem Cells and Regenerative Medicine Yeo, Jingjie; Cornell University, Sibley School of Mechanical and Aerospace Engineering;

Thermo- and Ion-responsive Silk-elastin-like Proteins and Their Multiscale Mechanisms

Haoyuan Shi[1], Ting Ji[2], Chenxi Zhai[1], Junting Lu[2], Wenwen Huang[2,3,4], Jingjie Yeo[1]**

[1]J[2] Lab for Engineering Living Materials, Sibley School of Mechanical and Aerospace Engineering, Cornell University, Ithaca, NY, 14853, United States.

[2]The Zhejiang University–University of Edinburgh Institute, Zhejiang University School of Medicine, Zhejiang University, Hangzhou 310058, China.

[3]Department of Orthopedics of the Second Affiliated Hospital, Zhejiang University School of Medicine, Zhejiang University, Hangzhou 310058, China.

[4]Dr. Li Dak Sum & Yip Yio Chin Center for Stem Cells and Regenerative Medicine, Zhejiang University School of Medicine, Zhejiang University, Hangzhou, China.

*Corresponding authors: wenwenhuang@intl.zju.edu.cn, jingjieyeo@cornell.edu.

Abstract:

Silk-elastin-like protein (SELP) is an excellent biocompatible and biodegradable material for hydrogels with tunable properties that can respond to multiple external stimuli. By integrating fully atomistic, replica exchange molecular dynamics simulations with detailed experiments, we predict and measure structural responses to changes in temperature and ion concentration of a novel SELP sequence, as well as a diazonium-coupled version. A single SELP molecule shrinks at high temperatures, whereas diazonium coupling decreases this thermo-responsiveness. Diazonium coupling weakens electrostatic interactions, leading to an insignificant ionic response in the single chain, while also decreasing gelation rates by reducing the number of exposed dityrosine crosslink sites and their solvent-accessible surface areas. With further data from our coarse-grained crosslinked SELP model and our experiments, we find that three effects are critical for SELP cluster's physical response to external stimuli: 1) the structural transition of

SELP under high temperature, 2) the geometry restraints in hydrogel networks, and 3) the electrostatic interactions between molecules. This molecular understanding of the thermal and ion response in single molecules of SELPs and their crosslinked networks may further improve and help innovate SELP's stimuli-responsive properties, creating significant opportunities for applications in biomedical devices and other engineering applications.

Keywords: silk-elastin-like protein (SELP), stimuli-responsive materials, replica exchange molecular dynamics, inverse temperature transition, electrostatic forces

Introduction

Soft, adaptive, and responsive biomaterials are extremely useful in engineering: one notable example is silk-elastin-like proteins (SELPs) that exhibit excellent biocompatibility, degradability, and dynamically tunable properties.[1] Engineered SELPs are exceedingly versatile for various processed morphologies, products, and applications that include gels, films, and particles for biosensors and drug delivery,[1–4] fibres for wound healing,[5,6] and scaffolds for tissue repair.[7,8]

SELPs are synthetic materials derived from recombinant DNA technology that create co-polymerized silk-like (GAGAGS) and elastin-like (G*X*GVP) domains. The silk-like domains mimic the *Bombyx mori* silkworm silk sequence that forms β-sheet crystallites to confer structural stability and mechanical stiffness. The elastin-like domains inherit the stimuli-responsiveness of elastin by exhibiting inverse temperature transitions when the temperature is raised above a lower critical solution temperature (LCST). In addition, the dynamic response towards other factors, such as ionic strength, pH, and light, can be tuned by altering the *X* residue or overall unit.[9,10] By incorporating both domains, SELPs possess favourable mechanical properties and stimuli-response tunability.

Numerous stimuli-responsive SELP hydrogels were synthesized experimentally and characterized by their deswelling capabilities after applying external stimuli.[2,9,11] However, the understanding of SELP behaviour in response to external stimuli remains nebulous at the nanoscale level: most detailed studies were for single-chain SELPs responding to changes in temperature.[9,12,13] Fully atomistic molecular dynamics (FAMD) simulations were most commonly used in tandem with advanced large-scale replica exchange (RE) methods[14] to obtain SELP conformations under various conditions.[15] Previous simulation results showed that a single

SELP molecule collapsed and bent when the temperature was above the LCST, exhibiting thermo-responsiveness.[9,12,13] This structural transition was impeded in larger clusters of SELP molecules.[13] However, the intertwined interactions in SELP clusters and how they affect the clusters' structural conformation are still unclear. These interactions critically influence the behaviours of SELP clusters in different external environments, and hence must be considered in SELP biomaterials possessing complex morphologies, such as hydrogels. Moreover, molecular mechanisms responsible for SELP's tunable response to other forms of stimuli, such as changes in ionic concentrations, are still unknown for both a single SELP molecule or SELP clusters.

Here, we combined molecular modelling with experiments to probe the structural transitions due to changes in temperature and ion concentrations for a novel, recombinantly synthesized SELP with the sequence $[(GAGAGS)_2(GVGVP)_4(RGYSLG)(GVGVP)_3]_{10}$ (Fig. 1). This SELP with thermo- and ion-response exhibits versatile biomedical applications, especially as biotherapeutic molecules. For example, the use of thermo-sensitive SELP products, like hydrogels, can target the release of drugs at the tumour site,[16] whereas, with ion-sensitive, they can assist wound regeneration or antibacterial activity.[17] Moreover, diazonium coupling modification is a facile experimental method to tailor the structure and hydrophilicity by substituting the tyrosine phenolic side chains with a diazonium salt.[18] This modification may further tune SELP's LCST and stimuli-responsiveness and guide the rational design and control of SELP with potential biomedical applications, such as nanobots or soft robotics. Thus, we also applied both simulation and experimental methods to analyze the properties of an aryl diazonium coupling of SELP with sulfonate group, abbreviated as Azo-SELP (Fig. S1a, ESI†), which can increase water solubility, promote cell clustering,[18] and provide binding sites for charged proteins or lipids.[19]

This study addressed two significant problems. First, to determine the mechanisms for structural changes caused by increases in temperature or the addition of ions, we applied FAMD to obtain the configuration of individual SELP and Azo-SELP molecules below and above the LCST, with and without ions added. The gelation rates of SELP and Azo-SELP were tested experimentally and compared to our molecular models, thereby verifying the effects on gelation rates by the number of exposed dityrosine crosslink sites and their solvent accessibility. These results can further guide SELP modification to design a tunable SELP with controllable LCST and gelation rates for broader applications in the field of biomedical engineering. Second, we characterized the thermal and ion response of SELP clusters with greater computational efficiency by mapping the SELP FA model to create a crosslinked CG model. By combining both experimental studies and the efficient conformational sampling of this crosslinked CG model, we observed how molecular geometric restraints and intermolecular electrostatic potential that, only in the crosslinked SELP cluster, affected the behaviours of individual SELP molecules within the cluster and of the whole cluster. Understanding the interactions of SELP molecules within a hydrogel cluster can spur further innovations in the properties of SELP-based materials through predictive design.

Block	Sequence	Function
Silk	GAGAGS	Confer structural stability and mechanical stiffness.
Elastin	GXGVP	Exhibits dynamic tunable responses.

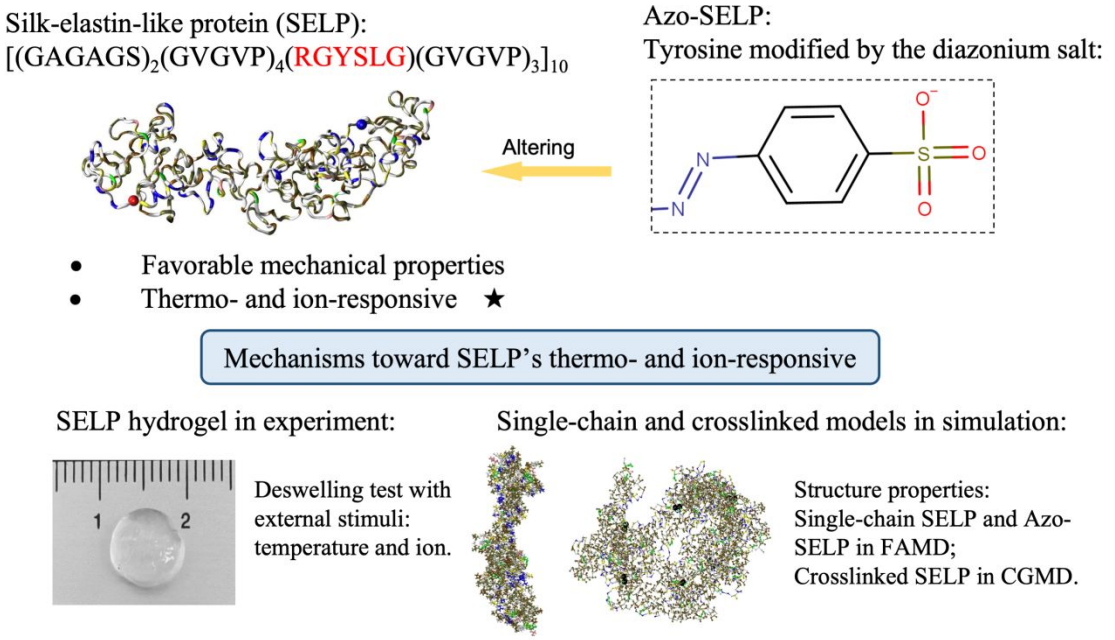

Fig. 1. The SELP in this work created co-polymerized silk-like (GAGAGS) and elastin-like (GXGVP) domains with a 1:4 ratio and a functional group RGYSLG, exhibiting favourable mechanical properties and thermo- and ion-responsive. Azo-SELP with tyrosine modifications can alter the responsiveness. Schematics of combining computational and experimental models provide a comprehensive understanding of macroscale and molecular mechanisms associated with the thermo- and ion-responsive deswelling of SELP hydrogels.

Results and discussions

Molecular behaviours of SELP and Azo-SELP under applied stimuli

The LCSTs of SELP and Azo-SELP were determined by monitoring the absorbance of the protein solutions at 350 nm as a function of temperature in the range of 273 to 373 K on a UV–vis spectrophotometer. As shown in Fig. 2a and b, SELP and Azo-SELP exhibited LCSTs at 298 ± 3 K and 313 ± 4 K, respectively, signifying that modifying tyrosine with the diazonium group escalated the LCST of SELP. These results were consistent with the previous study that the LCST could be tuned by adjusting the ratio between hydrophobic and hydrophilic groups,[2] and more hydrophilic derivatives led to higher LCST.[3] Thus, the LCST of Azo-SELP was higher since the sulfonic acid groups in modified tyrosine were hydrophilic. Moreover, the structural transformation in Azo-SELP was suppressed, as inferred by the substantially flatter absorbance curve in the Azo-SELP solution, indicating lower sensitivity of Azo-SELP response to changes in temperature. Thus, finely adjusting the number of modified tyrosines in SELP sequences can be a useful method for controlling the LCST as well as the thermal responsiveness of SELP.

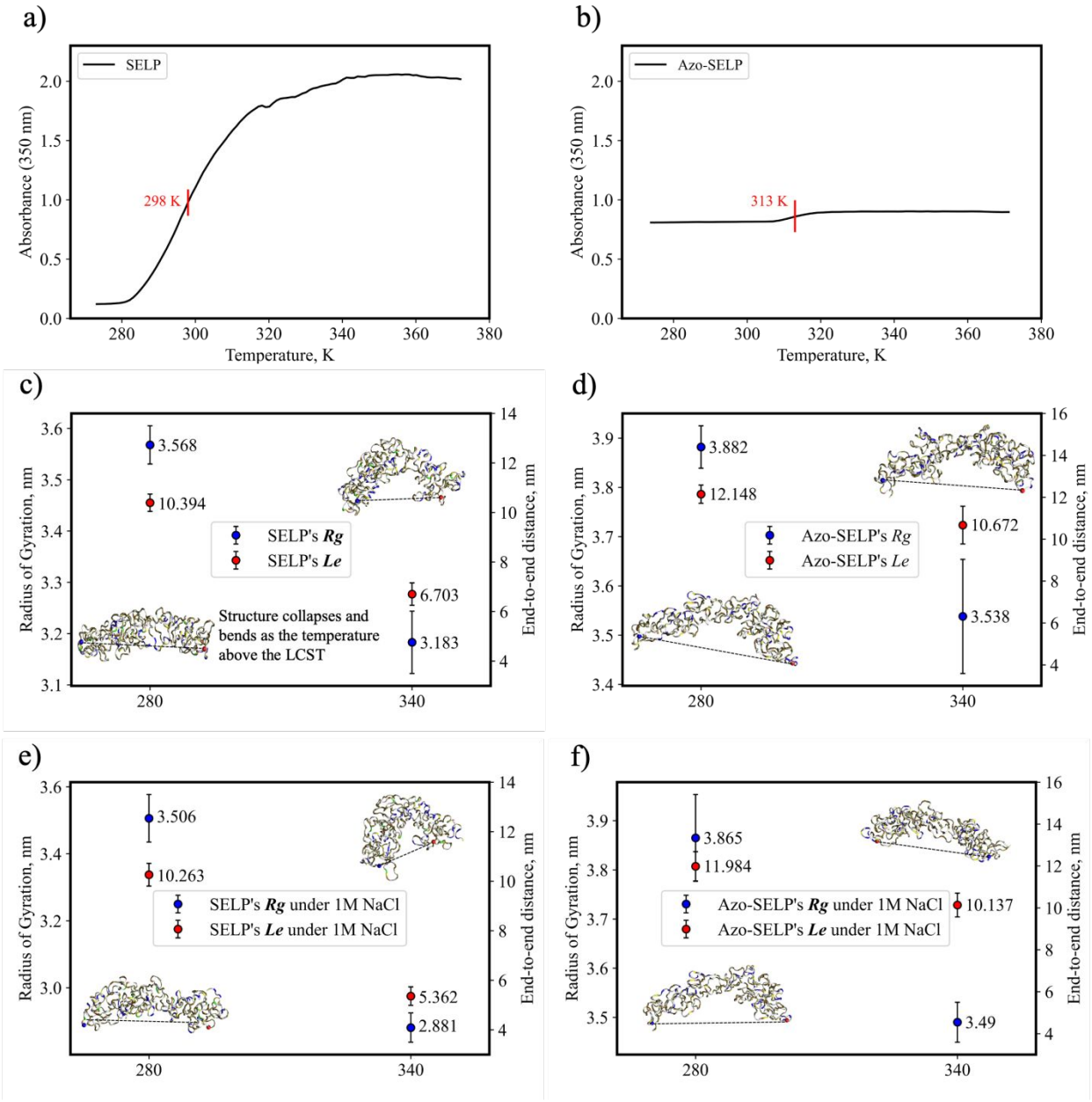

Fig. 2. Turbidity profiles of a) SELP and b) Azo-SELP indicate that adding diazonium groups in the tyrosine side chains escalated the range of LCST and diminished thermal responsiveness. The FAMD models captured the structural conformations of c) SELP and d) Azo-SELP under pure water, and e) SELP and f) Azo-SELP under 1M NaCl solution at 280 K and 340 K in terms of the radius of gyration (R_g) and end-to-end distance (L_e).

To unravel the molecular mechanisms underlying the thermal response of SELP and Azo-SELP, we applied FAMD with TIGER2 REMD sampling methods[20] to explore the protein conformations below and above the LCST at 280 K and 340 K respectively. We also further analyzed SELP and Azo-SELP responses to higher ion concentrations of 1M NaCl at these two temperatures. The full simulation schemes are in the Methods section and Fig. S4 (ESI†). Two fundamental metrics, the radius of gyration (R_g) and end-to-end distance (L_e), captured each protein's essential geometric features. The Azo-SELP structure had an 8.80 % larger R_g and 16.88 % larger L_e ($p < 0.0001$) than the SELP (Fig. 2c and d). However, the R_g and L_e of SELP decreased by 10.79 % and 35.31 % ($p < 0.0001$) respectively at the higher temperature of 340 K, signifying structural collapse and bending when the temperature was above the LCST. Such phenomena are consistent with elastin proteins[21] as well as other types of SELP in previous simulation studies.[9,12,13] In contrast, the R_g and L_g of Azo-SELP only reduced by 8.86 % and 10.80 % ($p < 0.0001$) at 340 K respectively. These shrinkages were much less than those of SELP, hence firmly reinforcing the flatter absorbance curves of the protein solutions in our experimental results.

We further determined that only SELP at high temperatures exhibited ionic responsiveness in 1M NaCl solution, where the R_g and L_e reduced by 9.49 % and 20.01 % ($p < 0.0001$) respectively (Fig. 2e and f), compared to the structures solvated in pure water. In comparison, these geometric properties of SELP at the low temperatures, as well as of Azo-SELP at both temperatures, did not change very much. To investigate this interesting variation in ionic responsiveness, we first explored the distribution and properties of charged groups in SELP and Azo-SELP, which tended

to bind ions in solution. The charged groups included -NH_2^+ in arginine, populating the SELP and Azo-SELP, and sulfonate groups in modified tyrosines within Azo-SELP that neutralized the total charge. As shown in Fig. 3a, SELP's -NH_2^+ groups were exposed to the environment, whereas those in Azo-SELP tended to be buried and ionic bonding with modified tyrosine's sulfonate groups. These results were consistent with the solvent-accessible surface area (SASA) of charged groups in Fig. 3b, showing that around 70 % of -NH_2^+ and sulfonate groups were within 10 Å, regarded as interacting, and more than 50 % reduction of SASA in Azo-SELP's -NH_2^+ groups than SELP's. Although Azo-SELP contained more charged groups and adding 1M NaCl caused more exposure of charged group, the number of ions surrounding charged groups and ion-protein binding energy in Azo-SELP were still lower than in SELP (Fig. 3b). These results unravelled the weaker interaction between protein and ions in Azo-SELP than SELP.

Despite this, more exposed charged groups under salt environments may endow Azo-SELP with targeted attachment capabilities on a charged surfaces such as cell lipid membranes. To assess this possibility, we calculated the surface charge distribution of SELP and Azo-SELP at the two temperatures using APBS Electrostatics Plugin,[22] with and without 1M NaCl. A visual comparison of the charge distribution maps revealed substantial differences between the SELP with and without the 1M ion environment (Fig. 3c and d). In a pure water environment, the exposed surface of SELP is almost entirely blanketed by positive charges at both temperatures owing to the positively charged amino acid, arginine, populating the SELP. Therefore, adding ions greatly weakened the positive charge distributed on the surface, thereby reducing the electrostatic repulsion. In terms of a single molecule, SELP had a curved structure above the LCST due to the strong influence of intramolecular electrostatic repulsion. In contrast, SELP

resembled a rod-like structure below the LCST as it was hardly affected by such interactions. This contrast explained why SELP continued to collapse and shrink above the LCST once the intramolecular electrostatic repulsion was weakened by adding ions. However, modifying SELP with negatively charged diazonium groups neutralized the structure of Azo-SELP, thus decreasing the positive charge distribution on the surface. Therefore, the Azo-SELP exhibited diminished sensitivity to the presence of ions. Meanwhile, the ionic bonding in Azo-SELP between different elastin blocks impeded the functionality of the four consecutive elastin blocks. These ionic bonds also suppressed the thermos-responsiveness of Azo-SELP and led to a stable rod-like structure at a higher temperature.

a)

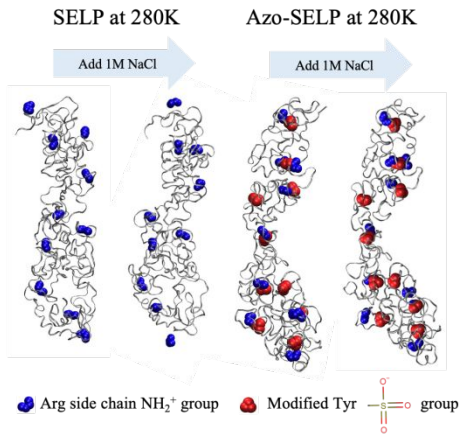

b)

	SELP		Azo-SELP	
	Water	1M NaCl	Water	1M NaCl
SASA of (Å²)	237.656 ± 43.860	246.939 ± 42.713	71.756 ± 22.850	123.618 ± 35.943
SASA of (Å²)	N/A	N/A	23.398 ± 17.090	64.046 ± 26.875
The percentage of - interactions (%)	N/A	N/A	74.899 ± 1.000	69.469 ± 5.705
Number of Cl^- surrounding	N/A	10.588 ± 2.741	N/A	5.713 ± 2.173
Number of Na^+ surrounding	N/A	N/A	N/A	3.764 ± 1.784
Ion-protein binding energy (kcal/mol)	N/A	-763.005 ± 175.924	N/A	-563.590 ± 136.680

c)

d)

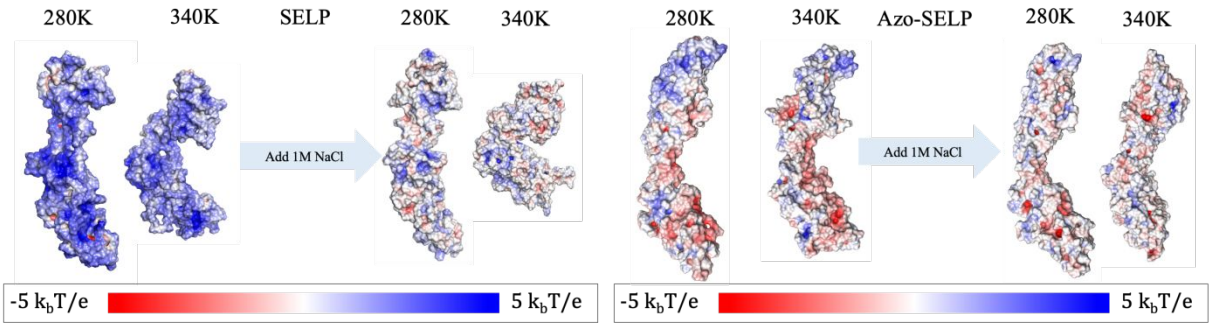

Fig. 3. a) The distribution of charged groups, including Arg side chain NH_2^+ group and modified tyrosine sulfonate group, in representative SELP and Azo-SELP. b) Some properties of charged

groups in SELP and Azo-SELP under water and 1M NaCl solution. Surface charge distributions of c) SELP and d) Azo-SELP at these temperatures with and without 1M NaCl. The red areas represent a local net negative charge, the blue areas represent positive, and the white areas represent uncharged. The unit is k_bT/e, where k_b is the Boltzmann constant, T is the temperature, and e is the electron charge.

In addition to decreasing the thermo- and ion-responsiveness, modifying with diazonium groups also alter the gelation dynamics of SELP into a hydrogel. HRP-mediated crosslinking reactions were performed in 5 % protein solutions to test the gelation of SELP and Azo-SELP. Before adding HRP and H_2O_2, the solutions were homogeneous for both samples. After mixing HRP and H_2O_2 for 12 hours, the 5 % SELP solution transformed to hydrogel while the Azo-SELP solution remained liquid (Fig. 4). FAMD simulation helps us verify and explain these phenomena. The gelation rate is related to the exposure of dityrosine crosslink sites that are ortho and meta carbons in the phenol group of tyrosine. Thus, the SASA of dityrosine crosslink sites and the number of exposed dityrosine crosslink sites were analyzed, as detailed in the ESI†. The results showed that the sites' SASA and the exposed sites in Azo-SELP reduced by 37.20 % and 42.96 % ($p < 0.0001$) respectively (Table 1). This was also because the number of crosslink sites in Azo-SELP is only three-fourths SELP since one was connected to diazonium groups. Therefore, the gelation of Azo-SELP is significantly reduced.

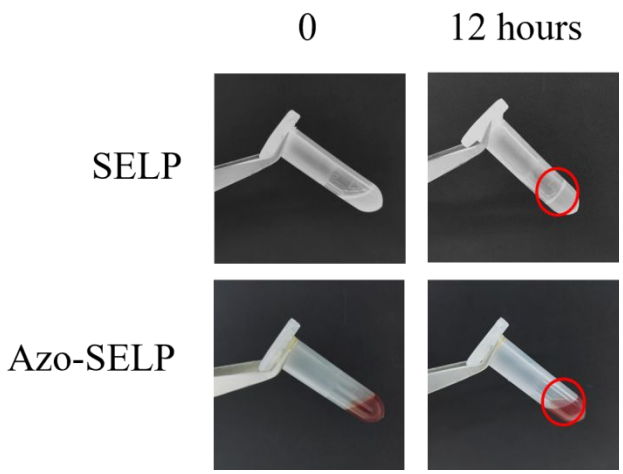

Fig. 4. Picture showing the visualization of the SELP hydrogel after mixing HRP and H_2O_2 at room temperature and incubating for 12 hours, whereas the Azo-SELP solution remained liquid.

Table 1. The SASA of dityrosine crosslink sites and the number of exposed dityrosine crosslink sites for the representative SELP and Azo-SELP structures.

	SELP	Azo-SELP
R_g (nm)	3.506 ± 0.037	3.882 ± 0.043
L_e (nm)	10.394 ± 0.348	12.148 ± 0.436
$SASA_{site}$ (Å^2)	156.190 ± 15.577	98.095 ± 9.681
Exposed site	14.587 ± 1.880	8.320 ± 1.187

Interactions in crosslinked SELP clusters contribute to thermal and ion-responsiveness

To further characterize the SELP size variations as temperature increases or adding ions in the crosslinked SELP, we mapped a CG model from the FA model based on the Martini 3.0 forcefield, the latest version of a widely-used CG scheme in biomaterials simulation.[23] In the Martini CG mapping scheme, the SELP FA model containing 6,133 atoms will simplify into 840 Martini CG beads (Fig. 5), significantly increasing computational efficiency. We validated the Martini CG scheme in our FA model (see Methods section and Fig. S5 in ESI†). Using this single-chain SELP CG model, a CG crosslinked model consisting of 6 SELPs was generated to mimic the dityrosine-crosslinked SELP hydrogel (see Methods section). This crosslinked model was used to explore the interactions between each chain within the cluster. The single-chain and crosslinked models were discretely simulated in the temperature range of 280 K to 340 K in increments of 20 K. For comparison, in our experiments, 5% SELP hydrogel was equilibrated in deionized water at different temperatures, as well as in 1M NaCl solution at 280 K to examine the deswelling. The deswelling degree is defined as the ratio of hydrogel weight under a specific experimental condition to its original weight in deionized water at 277 K.[9]

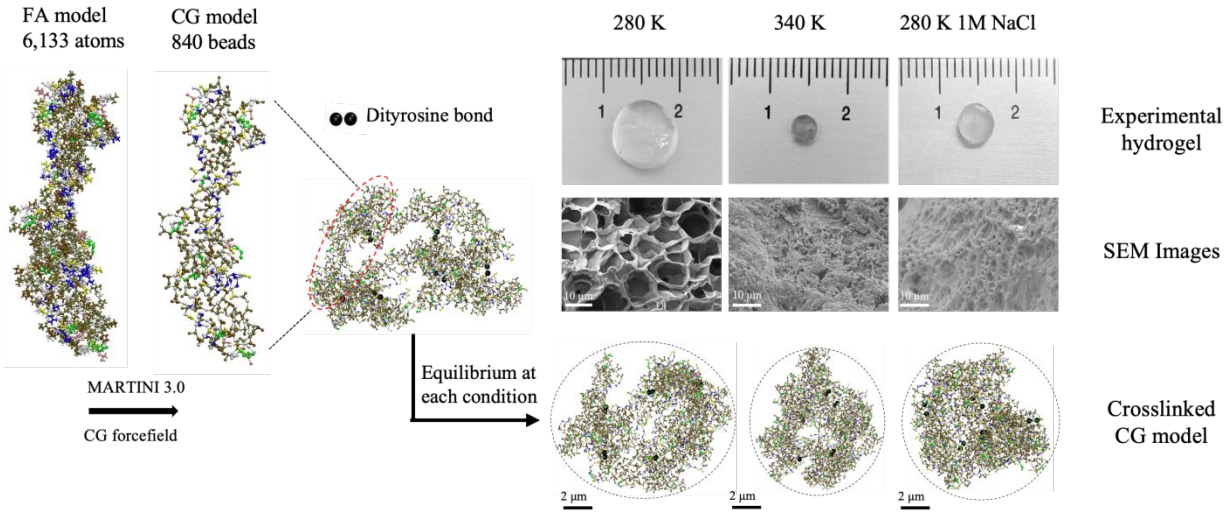

Fig. 5. The crosslinked CG models, SEM images, and SELP hydrogel showed that all metrics of the R_g, pore sizes, and volume sizes decreased as the temperature increased from 280 K to 340 K or added 1M NaCl.

The chain aggregation in the crosslinked CG model led to structural shrinkage when either increasing the temperature or adding ions (Fig. 5), with R_g decreasing by 12.76 % and 9.46 % respectively. These observations were consistent with the noticeable shrinkage in both the hydrogel dimensions that were synthesized, as well as the pore sizes in the corresponding SEM images. Moreover, both single-chain and crosslinked CG models under various temperatures showed significantly reduced deswelling above the LCST, with their R_g decreasing by 11.57 % and 12.76 % at 340 K respectively (Fig. 6a, green and blue line). The same phenomena appeared in our experimentally synthesized SELP hydrogel, where the hydrogel weight decreased by 71.59 % at 340 K (Fig. 6b). Different degrees of thermal response between our experimental and simulation data arose because the CG models cannot capture the aggregation of multiple SELP clusters into even larger clusters with more complex stacking, and the crosslink density cannot be precisely determined and modelled. However, the average R_g for chains in the crosslinked model only showed a minimal reduction of 5.26 % from 280 K to 340 K with almost no changes at some temperatures (Fig. 6a, orange line), substantially smaller than the change in the single-chain model (Fig. 6a, green line). This inability to shrink implied that the crosslinked SELP impeded each chain's structural transition at high temperatures individually (i.e. geometrically restrained), but the whole crosslinked structure still underwent a phase transition due to the chains' collective aggregation into a tightly bound cluster.

We also compared the ion responsiveness of both the CG crosslinked model and the SELP hydrogel. From our CGMD results (Fig. 6a, star markers at 280 K), the crosslinked model is much more sensitive to ions than the single-chain model, with the R_g respectively reducing by 9.46 % and 1.73 % at 1M NaCl solution under 280 K, which is due to the reduced repulsion between molecules (Fig. 3c). The average R_g for each of the six molecules in the crosslinked model also decreased by 4.31 %. In our experiments (Fig. 6b, star marker at 280 K), the SELP hydrogel also exhibited a considerable reduction of 66.45 % in weight at 1M NaCl solution under 280 K.

Thus overall, we found three direct molecular mechanisms in the SELP hydrogel that governed its responses to changes in temperature and ionic concentration: 1) the structural transition of SELP under high temperature, 2) the geometry restraints in hydrogel networks, and 3) the electrostatic interactions between molecules. As the SELP hydrogel was exposed to a temperature above the LCST, the reversible transition in single molecules triggered a shrinkage of the hydrogel in volume. However, the amount of structural transitions in a single SELP was strongly inhibited since the motion of individual SELP molecules was limited by the dense packing of the molecules and the intermolecular dityrosine bonds. In addition, different mechanisms were exhibited in the SELP hydrogels in response to changes in ionic concentrations. Ions weakened and screened intermolecular electrostatic forces and induced molecular aggregation. During this process, geometry restraints may instead increase the deformation of a single molecule, as the average R_g for each SELP chain in the crosslinked model increased compared to the single-chain model at 1M NaCl solution under 280 K (Fig. 6a, star markers at 280 K).

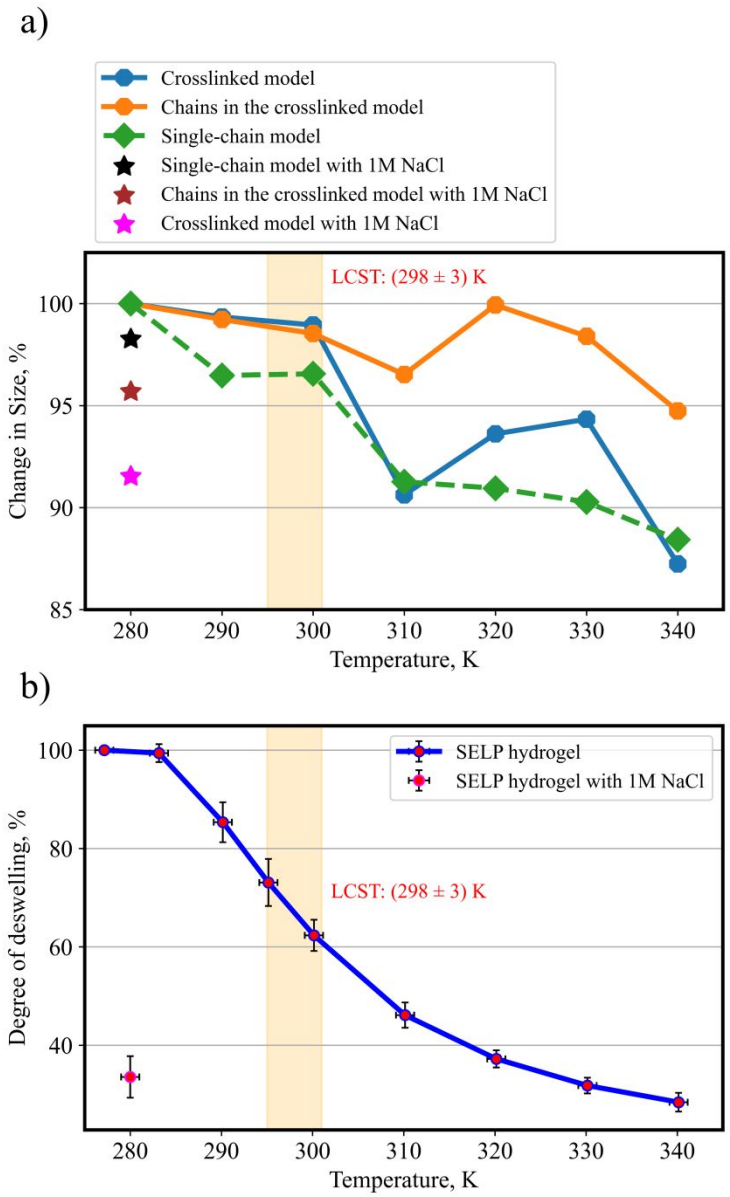

Fig. 6. (a) Variations in the R_g of the CG models when increasing temperature or adding 1M NaCl, including the single-chain CG model (green line and black star), the crosslinked CG model (blue line and magenta star), and chains in the crosslinked CG model (orange line and brown star). The results showed that the geometry restraints strongly affected the transitions of SELP chains in the crosslinked model. b) The experimental deswelling tests for SELP hydrogel in terms of the SELP's weight. Both the crosslinked CG model and the single-chain CG model

showed significantly reduced deswelling above the LCST, in good correlation with the trends from our experiments.

Conclusions

SELP-based biomaterials exhibit not only biocompatibility and biodegradability but also tunability of their response to external stimuli. Integrative experimental and computational approaches can help explore the mechanism of various responsiveness and optimize the design of SELP sequences with controllable responsive properties.

In this work, we first constructed MD models for novel sequences of SELP and diazonium coupled SELP, Azo-SELP, to explore their single-molecule responsiveness to changes in temperature and ionic concentration. Experimental DSC data showed a distinct LCST of SELP at 298 ± 3 K. Azo-SELP exhibited a flatter curve with LCST at 313 ± 4 K, signifying a structural transformation was not apparent. These results were consistent with simulations, where the R_g and L_e for SELP decreased 10.79 % and 35.31 % at 340 K above the LCST respectively, whereas for these metrics decreased by 8.86 % and 10.80 % respectively in Azo-SELP. Only SELP at 340 K responded to increased ionic concentration of 1M NaCl, where R_g and L_e decreased by 9.49 % and 20.01 % respectively. We explained these differences by determining that positive charges almost entirely covered the exposed surface of SELP due to the positively charged arginine, and SELP at 340 K had a curved structure heavily affected by intramolecular electrostatic repulsion. As a result, adding ions weakened the positive charge distributed on the surface, thereby reducing the electrostatic repulsion and leading to shrinkage. However, SELP resembled a rod-like structure at 280 K, which was barely affected by such interactions and thus was not sensitive to changes in ionic concentration. Azo-SELP possessed the same amounts of negatively charged sulfonate groups as positively charged arginines, rendering the structure neutral. In addition, the reduced SASA and number of surrounded ions in charged groups led to a weak ion-protein

binding energy in Azo-SELP. Hence, the surface charge distribution did not change significantly after adding ions. Future studies will focus on different ratios of diazonium coupling modification in SELP to design SELPs that exhibit controllable LCST and optimal sensitivity to different external stimuli.

Besides ion and thermal responsiveness, our experiments showed that the gelation rate was inhibited in Azo-SELP. The reason was that the potential dityrosine crosslink sites in SELP were occupied by the diazonium group, significantly decreasing the SASA of dityrosine crosslink sites and the number of exposed dityrosine crosslink sites. CGMD simulations of individual and crosslinked SELP were performed together with experimental synthesis and characterizations to investigate the interactions in the SELP cluster. Both individual and crosslinked SELP showed decreasing in R_g by 11.57 % and 12.76 % at 340 K, respectively, consistent with the SELP hydrogel with an observed shrinkage. However, the average R_g of SELP chains in the crosslinked model only showed a minimal reduction of 5.26 % from 280 K to 340 K, substantially smaller than the change in the single-chain model. These results revealed that the reversible transition in single molecules triggered a shrinkage of the hydrogel in volume, but the degree of the transition in a single SELP was inhibited. These geometry restraints were caused by closely packed molecules and limited molecular realignment imposed by the intermolecular dityrosine bonds. Our CGMD simulations also showed R_g shrinking by 9.46% for crosslinked SELP when exposed to 1M NaCl due to the weakening of intermolecular electrostatic repulsion.

Overall, reversible transition behaviour and electrostatic potential govern the SELP response to changes in temperature and ionic concentration respectively. Understanding such interactions in

the thermo- and ion-responsiveness of SELP hydrogels provides huge potential in designing, optimizing, and customizing SELP hydrogels for advanced biomaterials applications. Furthermore, our integrative experimental and computational approaches can potentially be applied to other novel SELP sequences with new forms of stimuli-responsiveness, thereby paving the way towards innovative SELP-based, multistimuli-responsive biomaterials.

Materials and methods

Synthesis of Polymers

SELP was synthesized using recombinant DNA technology and purified by the inverse temperature transition cycling (ITC) method as described previously.[24] Briefly, the SELP multimer genes of $[(GAGAGS)_2(GVGVP)_4(RGYSLG)(GVGVP)_3]_{10}$ were inserted into a tailor-made expression vector, pET-19b3, and expressed by fermentation under the T7 promoter in Escherichia coli strain BL21 Star (DE3) (Invitrogen, Carlsbad, CA). After purification by the ITC method, the purity of the protein was determined by sodium dodecyl sulfate-polyacrylamide gel electrophoresis (SDS-PAGE). Azo-SELP was prepared using a diazonium coupling reaction following the previous published method.[18] More than 90% of the tyrosine moieties in SELP were modified by diazonium. According to the absorbance spectra of UV–Vis spectroscopy (Fig. S2), tyrosine absorption at 280 nm in the native protein decreases after modification. Likewise, a strong absorption corresponding to the newly formed azobenzene chromophore can be seen at 338 nm with a shoulder at 390 nm. The level of diazonium modification was calculated based on Beer's Law.[18]

Preparation of SELP Hydrogels

SELP hydrogels were obtained using our previous procedures.[25] Briefly, the lyophilized SELP powder was dissolved in deionized water at 277 K for 4 h to form a 5 % (by weight) SELP stock solution. Then, 3 μL of 40 mg/mL horseradish peroxidase (HRP) stock solution and 1 μL of 3 % H_2O_2 solution were added to initiate the crosslinking reaction. The mixture was incubated overnight at 277 K to form 5 % SELP hydrogels. The formed SELP hydrogels were equilibrated

in deionized water at 277 K. In the deswelling tests, we also tested different concentrations of 2.5 % and 10 % SELP stock solution and obtained similar results.

UV−Vis Spectrophotometry

The LCST of 0.25 mg/mL protein solutions were characterized by a Shimadzu UV-2600 UV-vis spectrophotometer equipped with a Tm analysis accessory TMSPC-8 (Shimadzu, Kyoto, Japan). Temperature scans were measured at 350 nm in the range of 273 to 373 K at a rate of 278 K/min. The baseline scans were taken with deionized water under the same condition and subtracted from the sample scans. The lower critical solution temperatures (LCSTs) were determined as the temperature corresponding to the point with the maximum slope in the turbidity profile.

Scanning Electron Microscopy

The microstructures of SELP hydrogels were observed using a Hitachi SU8010 field-emission scanning electron microscope (Hitachi Ltd, Tokyo, Japan). Images were taken with SE2 detectors at 5.00 kV.

Fully atomistic molecular simulation setup

The SELP structure in this project is a 10-monomer alternating silk-elastin chain with the sequence of $[(GAGAGS)_2(GVGVP)_4(RGYSLG)(GVGVP)_3]_{10}$ and constructed by the UCSF Chimera software[26] with a fully extended structure. The diazonium coupling of SELP added a diazonium group containing diazene and sulfonic acid to the ortho-carbon of the phenol group in tyrosine (Fig. S1a). All simulations are in NAMD 2.13 software[27] using the CHARMM36 forcefield[28]. In addition, the parameters of diazene moieties in Azo-SELPs are generated using

the Force Field Toolkit (FFTK),[29] and the sulfonic acid was using the CHARMM General force field (CGenFF)[30] as in Fig. S1b (ESI†). Both simulations and experiments explored the SELP with identical sequences.

The FAMD simulations were based on our well-established procedures[9,12,13] and illustrated in Fig. S4 (ESI†). After energy minimization through conjugate gradient algorithm, the conformations of these proteins are then sampled using the advanced MD method of temperature intervals with global exchange of replicas (TIGER2)[31], an empirical enhanced sampling method adapted from traditional replica exchange (RE) MD to reduce the enormous computational costs. In the TIGER2 approach, multiple replicas of the same model system are simulated at different temperatures, where the total number of replicas are chosen by the user, independent of the system size. This independence is feasible as the TIGER2 method performs the Monte-Carlo based swaps between replicas only after quenching all replicas to the same baseline temperature. Full details of the forcefield and the TIGER2 methodology are laid out in the ESI†. We first performed the implicit TIGER2 method for the SELP using in Generalized Born implicit solvent (GBIS).[32] Eight replicas were chosen with temperatures exponentially distributed from 280 K to 480 K. The timestep was set to 4 fs, as we partitioned the mass of heavy atoms into the bonded hydrogen atoms.[33] We performed 10,000 cycles of replica swaps, equaling a simulation time of 600 ns for each replica, hence 4.80 μs in total, for both SELP and Azo-SELP calculations. Each sampling cycle contains 500 steps for heating, 12,000 steps for sampling, and 2,500 steps for quenching. Then, we performed another 3,000 cycles of replica swaps, equaling 180 ns of simulation time for each replica and 1.44 μs in total, with the same settings, but different temperature ranges from 280 K to 400 K. Subsequently, using GROMACS analysis tools[34] with

root-mean-square deviation (RMSD) of 6 Å, K-means clustering was performed on the structural ensembles from the last 1,000 exchanges at the baseline replica to obtain equilibrated structures. We then explicitly solvated this lowest-energy representative silk structure in a water box with fully periodic boundary conditions. After energy minimization through conjugate gradient algorithm, two equilibration stages were implemented (1 ns NVT simulation followed by 1 ns NPT simulation) with harmonic constraints to alpha carbons and a timestep of 1 fs. Langevin dynamics[35] and Nosé-Hoover Langevin piston[36] were used for temperature and pressure control at 280 K and 1.013 bar respectively. Rigid bonds were used with the SHAKE algorithm.[37] Particle-mesh Ewald (PME) method was used to calculate long-range electrostatic interactions.[38] Finally, we carried out the TIGER2 hybrid solvent with water shell (TIGER2hs)[20] with eight exchange replicas and one water shell replica, starting from the dissolved SELP after two equilibration stages. In shell replica, the SELP and Azo-SELP model contained 1,022 and 1,047 water molecules respectively. The TIGER2hs method is a significant improvement over TIGER2. Each replica is run with explicit solvents in this method, but the potential energies for exchanges are determined in an implicit solvent environment in tandem with the closest shell of explicit water molecules. This hybrid method compensates for effects not represented by fully implicit solvents, e.g., polarization. In this simulation, the temperature ranged from 280 K to 340 K to obtain the stable conformation at 280 K, and from 340 K to 400 K to obtain the stable conformation at 340 K. The timestep was 2 fs, and each sampling cycle contained 500 steps of heating, 4,500 steps of sampling, and 2,500 steps of quenching. We performed 3,000 cycles of replica swaps, i.e., 45 ns of simulation time for each replica and 360 ns in total, for both SELP and Azo-SELP calculations at each temperature range. After using K-means clustering with the same settings, the conformation of representative SELP and Azo-SELP were chosen from the

most populated cluster. The TIGER2hs simulation scheme was then repeated with 1M NaCl to explore the response of SELP to ions.

Coarse-grain molecular simulation setup

After the extensive FAMD simulations, the representative structures of the SELP molecule under various conditions were coarse-grained using the scheme from the Martini 3.0 "open beta" version (v.3.0.b.3.2) CG forcefield (http://cgmartini.nl/),[23] and simulated via GROMACS 2020 software.[34] The structure was generated using the martinize.py script with the side-chain dihedral corrections script from the Martini 3.0 package. In Martini 3.0 forcefield, around four heavy atoms with their hydrogens are mapped into one CG bead, parametrized using a top-down approach.[23] Therefore, the computing system can be significantly simplified, e.g., 6,133 atoms in the SELP mapping to 840 CG beads, and apply large timestep, e.g., 20 fs. All CG models were run for 20 ns for validation against the FA models (Fig. S5, ESI†).

To simulate the transition of the SELP CG model, we used the SELP CG model at 280 K as a starting structure and ran 500 ns simulations in a pure Martini water box in the temperature range of 280 to 340 K with increments of 10 K. Although the backbone beads in Martini 3.0 no longer depend on the secondary structure, extra constraints exist in backbone angles and dihedrals for secondary structures. Thus, we mapped CG to the FA model via CHARMM-GUI[39] Martini Maker[40] every 100 ns and ran for 2 ns FAMD simulations with CHARMM 36 forcefield[28] for relaxation and mapped the final structure to the CG model initial structure for the next 100 ns CGMD simulation. The same CGMD simulation scheme was used in the 1M NaCl Martini solution for SELP at 280 K, starting from the SELP CG model at 280 K.

449

450 To simulate the dityrosine-crosslinked SELP, we built a six-SELP cluster with six dityrosine
451 bonds. The SELP in this model was the CG model under 280 K, and the dityrosine-crosslinked
452 sites were TC4 beads of tyrosine in residue 235 for one SELP and 447 for another SELP whose
453 SASA values ranked in the top three among all tyrosines and with more space for packing
454 molecules. The starting molecules were iteratively placed one after another using Packmol[41] and
455 TCL scripts with the dityrosine-crosslinked sites less than 10 Å. The simple harmonic spring
456 potential with the same parameters of backbone beads interaction was used to mimic dityrosine
457 bonding. The same simulation schemes as in the single CG model were used in the crosslinked
458 CG model with 500 ns simulations in a pure Martini water box in the temperature range of 280 to
459 340 K with increments of 10 K. In the mapped FA model, dityrosine bonds between two ortho
460 carbons corresponded to CG dityrosine bonds were added into the bond information and
461 simulated with CHARMM parameters. The same CGMD simulation scheme was used in the 1M
462 NaCl Martini solution at 280 K for crosslinked CG model, starting from the equilibrated
463 crosslinked CG model in pure Martini water.

464

465 Molecular dynamics data analysis tools

466 The radius of gyration (R_g) of the SELP and Azo-SELP were analyzed using GROMACS
467 analysis tools.[34] The end-to-end distance (L_e) was defined as the distance between two C_α at both
468 ends respecting the central axis and calculated by TCL scripts. The R_g and L_e are average values
469 with standard deviation, calculated based on the most populated cluster. The SASA of
470 representative SELP and Azo-SELP structures were calculated by TCL scripts. All visualization

471 of molecules was performed using Visual Molecular Dynamics (VMD),[42] PyMol,[43] and in-house
472 TCL, Python, and Bash scripts.
473
474 Calculation of surface charge distribution
475 Surface charges for SELP were calculated using the Adaptive Poisson-Boltzmann Solver
476 (APBS) Electrostatics Plugin[22] in PyMOL (http://www.pymol.org)[43] under various conditions.
477

Data availability

The data supporting the findings of this study are available from the corresponding author upon request.

Author Contributions

H. S., C.Z., and J.Y. designed, performed, and analyzed the computational experiments. T.J., J.L., and W.H. designed, performed, and analyzed the physical experiments. All authors made the figures and wrote the manuscript.

Funding Sources

H.S., C.Z., and J.Y. acknowledge the support provided by the XSEDE program under Grant TG-MAT200004, TG-BIO210063, and computational resources provided by Graphite and G2 cluster from Cornell University. J.Y. acknowledges support from the US National Science Foundation (Grant No. 2038057), Cornell University's Cornell-China Center, and Cornell University's faculty startup grant. This work was also supported by National Natural Science Foundation of China (52003233), Natural Science Foundation of Zhejiang Province (LHDMZ22H300004), and Fundamental Research Funds for the Central University (2021XZZX040 and K20210261).

1 L. Chambre, Z. Martín-Moldes, R. N. Parker and D. L. Kaplan, *Advanced drug delivery reviews*, 2020, **160**, 186–198.

2 R. N. Parker, D. M. Cairns, W. A. Wu, K. Jordan, C. Guo, W. Huang, Z. Martin-Moldes and D. L. Kaplan, *Advanced Healthcare Materials*, 2020, **9**, 1–8.

3 R. N. Parker, W. A. Wu, T. B. McKay, Q. Xu and D. L. Kaplan, *Journal of functional biomaterials*, , DOI:10.3390/jfb10040049.

4 W. Huang, A. Rollett and D. L. Kaplan, *Expert opinion on drug delivery*, 2015, **12**, 779–791.

5 E. G. Roberts, N.-G. Rim, W. Huang, A. Tarakanova, J. Yeo, M. J. Buehler, D. L. Kaplan and J. Y. Wong, *Macromolecular bioscience*, 2018, **18**, e1800265–e1800265.

6 R. Machado, A. da Costa, V. Sencadas, C. Garcia-Arévalo, C. M. Costa, J. Padrão, A. Gomes, S. Lanceros-Méndez, J. C. Rodríguez-Cabello and M. Casal, *Biomedical materials (Bristol, England)*, 2013, **8**, 65009.

7 Z. Chen, Q. Zhang, H. Li, Q. Wei, X. Zhao and F. Chen, *Bioactive Materials*, 2021, **6**, 589–601.

8 W. Qiu, Y. Huang, W. Teng, C. M. Cohn, J. Cappello and X. Wu, *Biomacromolecules*, 2010, **11**, 3219–3227.

9 W. Huang, A. Tarakanova, N. Dinjaski, Q. Wang, X. Xia, Y. Chen, J. Y. Wong, M. J. Buehler and D. L. Kaplan, *Advanced Functional Materials*, 2016, **26**, 4113–4123.

10 X. Shen, H. Shi, H. Wei, B. Wu, Q. Xia, J. Yeo and W. Huang, *Frontiers in chemistry*, 2022, **10**, 881028.

11 O. P. Narayan, X. Mu, O. Hasturk and D. L. Kaplan, *Acta Biomaterialia*, 2021, **121**, 214–223.

12 A. Tarakanova, W. Huang, Z. Qin, D. L. Kaplan and M. J. Buehler, *ACS Biomaterials Science and Engineering*, 2017, **3**, 2889–2899.

13 J. Yeo, W. Huang, A. Tarakanova, Y. W. Zhang, D. L. Kaplan and M. J. Buehler, *Journal of Materials Chemistry B*, 2018, **6**, 3727–3734.

14 Y. Sugita and Y. Okamoto, *Chemical Physics Letters*, 1999, **314**, 141–151.

15 C. Zhai, T. Li, H. Shi and J. Yeo, *Journal of Materials Chemistry B*, 2020, **8**, 6562–6587.

16 H. Huang, X. Qi, Y. Chen and Z. Wu, *Saudi Pharmaceutical Journal*, 2019, **27**, 990–999.

17 M. Rudko, T. Urbaniak and W. Musiał, *Polymers*, 2021, **13**, 1641.

18 A. R. Murphy, P. St John and D. L. Kaplan, *Biomaterials*, 2008, **29**, 2829–2838.

19 R. J. Ouellette and J. D. Rawn, eds. R. J. Ouellette and J. D. B. T.-O. C. (Second E. Rawn, Academic Press, 2018, pp. 801–828.

20 N. Geist, M. Kulke, L. Schulig, A. Link and W. Langel, *Journal of Physical Chemistry B*, 2019, **123**, 5995–6006.

21 N. K. Li, F. G. Quiroz, C. K. Hall, A. Chilkoti and Y. G. Yingling, *Biomacromolecules*, 2014, **15**, 3522–3530.

22 E. Jurrus, D. Engel, K. Star, K. Monson, J. Brandi, L. E. Felberg, D. H. Brookes, L. Wilson, J. Chen, K. Liles, M. Chun, P. Li, D. W. Gohara, T. Dolinsky, R. Konecny, D. R. Koes, J. E. Nielsen, T. Head-Gordon, W. Geng, R. Krasny, G.-W. Wei, M. J. Holst, J. A. McCammon and N. A. Baker, *Protein Science*, 2018, **27**, 112–128.

23 P. C. T. Souza, R. Alessandri, J. Barnoud, S. Thallmair, I. Faustino, F. Grünewald, I. Patmanidis, H. Abdizadeh, B. M. H. Bruininks, T. A. Wassenaar, P. C. Kroon, J. Melcr, V. Nieto, V. Corradi, H. M. Khan, J. Domański, M. Javanainen, H. Martinez-Seara, N. Reuter, R. B. Best, I. Vattulainen, L. Monticelli, X. Periole, D. P. Tieleman, A. H. de Vries and S. J. Marrink, *Nature Methods*, 2021, **18**, 382–388.

24 Q. Wang, X. Xia, W. Huang, Y. Lin, Q. Xu and D. L. Kaplan, *Advanced Functional Materials*, 2014, **24**, 4303–4310.

25 Y. Wang, W. Huang, W. Huang, Y. Wang, X. Mu, S. Ling, H. Yu, W. Chen, C. Guo, M. C. Watson, Y. Yu, L. D. Black, M. Li, F. G. Omenetto, C. Li and D. L. Kaplan, *Proceedings of the National Academy of Sciences of the United States of America*, 2020, **117**, 14602–14608.

26 E. F. Pettersen, T. D. Goddard, C. C. Huang, G. S. Couch, D. M. Greenblatt, E. C. Meng and T. E. Ferrin, *Journal of computational chemistry*, 2004, **25**, 1605–1612.

27 J. C. Phillips, D. J. Hardy, J. D. C. Maia, J. E. Stone, J. V Ribeiro, R. C. Bernardi, R. Buch, G. Fiorin, J. Hénin, W. Jiang, R. McGreevy, M. C. R. Melo, B. K. Radak, R. D. Skeel, A. Singharoy, Y. Wang, B. Roux, A. Aksimentiev, Z. Luthey-Schulten, L. V Kalé, K. Schulten, C. Chipot and E. Tajkhorshid, *The Journal of chemical physics*, 2020, **153**, 44130.

28 J. Huang and A. D. J. MacKerell, *Journal of computational chemistry*, 2013, **34**, 2135–2145.

29 C. G. Mayne, J. Saam, K. Schulten, E. Tajkhorshid and J. C. Gumbart, *Journal of Computational Chemistry*, 2013, **34**, 2757–2770.

30 K. Vanommeslaeghe, E. Hatcher, C. Acharya, S. Kundu, S. Zhong, J. Shim, E. Darian, O. Guvench, P. Lopes, I. Vorobyov and A. D. J. Mackerell, *Journal of computational chemistry*, 2010, **31**, 671–690.

31 X. Li, R. A. Latour and S. J. Stuart, *Journal of Chemical Physics*, 2009, **130**, 1–9.

32 W. C. Still, A. Tempczyk, R. C. Hawley and T. Hendrickson, *Journal of the American Chemical Society*, 1990, **112**, 6127–6129.

33 C. W. Hopkins, S. Le Grand, R. C. Walker and A. E. Roitberg, *Journal of Chemical Theory and Computation*, 2015, **11**, 1864–1874.

34 M. J. Abraham, T. Murtola, R. Schulz, S. Páll, J. C. Smith, B. Hess and E. Lindahl, *SoftwareX*, 2015, **1–2**, 19–25.

35 J. C. Phillips, R. Braun, W. Wang, J. Gumbart, E. Tajkhorshid, E. Villa, C. Chipot, R. D. Skeel, L. Kalé and K. Schulten, *Journal of Computational Chemistry*, 2005, **26**, 1781–1802.

36 S. E. Feller, Y. Zhang, R. W. Pastor and B. R. Brooks, *The Journal of Chemical Physics*, 1995, **103**, 4613–4621.

37 V. Kräutler, W. F. van Gunsteren and P. H. Hünenberger, *Journal of Computational Chemistry*, 2001, **22**, 501–508.

38 U. Essmann, L. Perera, M. L. Berkowitz, T. Darden, H. Lee and L. G. Pedersen, *\jcp*, 1995, **103**, 8577–8593.

39 S. Jo, T. Kim, V. G. Iyer and W. Im, *Journal of Computational Chemistry*, 2008, **29**, 1859–1865.

40 Y. Qi, H. I. Ingólfsson, X. Cheng, J. Lee, S. J. Marrink and W. Im, *Journal of Chemical Theory and Computation*, 2015, **11**, 4486–4494.

41 L. Martínez, R. Andrade, E. G. Birgin and J. M. Martínez, *Journal of computational chemistry*, 2009, **30**, 2157–2164.

42 W. Humphrey, A. Dalke and K. Schulten, *Journal of Molecular Graphics*, 1996, **14**, 33–38.

43 Schrödinger, LLC, *The {PyMOL} Molecular Graphics System, Version~1.8*, 2015.